Optimization of return electrodes in neurostimulating arrays

2016 J. Neural Eng. 13 036010

(http://iopscience.iop.org/1741-2552/13/3/036010)

IOP Publishing Journal of Neural Engineering
J. Neural Eng. 13 (2016) 036010 (11pp) doi:10.1088/1741-2560/13/3/036010

Optimization of return electrodes in neurostimulating arrays

Thomas Flores[1,6], **Georges Goetz**[2,3], **Xin Lei**[4] **and Daniel Palanker**[2,5]

[1] Department of Applied Physics, Stanford University, Stanford, CA 94305, USA
[2] Hansen Experimental Physics Laboratory, Stanford University, Stanford, CA 94305, USA
[3] Department of Neurosurgery, Stanford University, Stanford, CA 94305, USA
[4] Department of Electrical Engineering, Stanford, CA 94305, USA
[5] Department of Ophthalmology, Stanford University, Stanford, CA 94305, USA

E-mail: tomflo@stanford.edu

Received 20 November 2015, revised 20 March 2016
Accepted for publication 21 March 2016
Published 21 April 2016

Abstract

Objective. High resolution visual prostheses require dense stimulating arrays with localized inputs of individual electrodes. We study the electric field produced by multielectrode arrays in electrolyte to determine an optimal configuration of return electrodes and activation sequence. *Approach*. To determine the boundary conditions for computation of the electric field in electrolyte, we assessed current dynamics using an equivalent circuit of a multielectrode array with interleaved return electrodes. The electric field modeled with two different boundary conditions derived from the equivalent circuit was then compared to measurements of electric potential in electrolyte. To assess the effect of return electrode configuration on retinal stimulation, we transformed the computed electric fields into retinal response using a model of neural network-mediated stimulation. *Main results*. Electric currents at the capacitive electrode-electrolyte interface redistribute over time, so that boundary conditions transition from equipotential surfaces at the beginning of the pulse to uniform current density in steady state. Experimental measurements confirmed that, in steady state, the boundary condition corresponds to a uniform current density on electrode surfaces. Arrays with local return electrodes exhibit improved field confinement and can elicit stronger network-mediated retinal response compared to those with a common remote return. Connecting local return electrodes enhances the field penetration depth and allows reducing the return electrode area. Sequential activation of the pixels in large monopolar arrays reduces electrical cross-talk and improves the contrast in pattern stimulation. *Significance*. Accurate modeling of multielectrode arrays helps optimize the electrode configuration to maximize the spatial resolution, contrast and dynamic range of retinal prostheses.

Keywords: multielectrode array, retinal prosthesis, neural stimulation, electrical stimulation, return electrode, modeling of electric field

(Some figures may appear in colour only in the online journal)

1. Introduction

In neural circuits, information processing and transmission is associated with changes in the cellular transmembrane potential, which allows for recording and introducing information via electrode arrays. Therapeutic applications of electro-neural interfaces in the central and peripheral nervous system are rapidly expanding [1, 2]. Cochlear implants [3] have seen the most remarkable success in sensory neuroprosthetics, while retinal implants [4, 5] and various motor prostheses [6–8] are constantly improving.

Degenerative retinal diseases, such as retinitis pigmentosa and age related macular degeneration, cause blindness due to loss of photoreceptors [9, 10], while the other two

[6] Author to whom any correspondence should be addressed.

retinal neural layers remain fairly intact [11–13]. Retinal prostheses are designed to reintroduce visual information into the neural system by electrically stimulating the surviving neurons [14]. Two distinct approaches to retinal prostheses have been developed: (1) the subretinal approach targets the first layer of neurons after the photoreceptors (inner nuclear layer, INL) composed primarily of bipolar and amacrine cells. (2) The epiretinal approach aims at stimulating the output cells of the retina (retinal ganglion cells, RGCs) whose axons form the optic nerve and relay visual signals to the brain. Epiretinal (Argus II, Second Sight Inc. [4, 15]) and subretinal (Alpha IMS, Retina Implant AG [16]) implants have been tested in clinical trials, and the Argus II is approved by FDA and CE for commercial use.

The subretinal and the epiretinal approach both rely on selectively stimulating the target neural layer. Direct stimulation of ganglion cells with epiretinal electrodes is designed to elicit an action potential in individual cells for each short ($<$1 ms) stimulus, and thereby could allow direct encoding of the ganglion cell output, completely bypassing the retinal neural network [17, 18]. Individual ganglion cells can be targeted with the epiretinal electrodes by careful shaping of the electric field [19]. Subretinal stimulation utilizes longer pulses (1–10 ms) to activate graded-response cells in the INL, whose signals propagate via a network of synaptic connections to the ganglion cells, where they trigger bursts of action potentials. Unlike epiretinal stimulation, which directly encodes the strength of the RGC response by the number of delivered pulses or their frequency, strength of the graded response in the INL is encoded by stimulus amplitude or duration. Network-mediated stimulation preserves some features of natural vision, such as flicker fusion at high frequencies, adaptation to static images, and nonlinear summation of subunits in the RGC receptive fields, which enables high spatial resolution [20].

To achieve spatial selectivity, both epiretinal and subretinal electrode arrays rely on precise shaping of the electric fields in tissue to achieve spatial selectivity. The desired percepts are complex, and models of electric field need to account for the distributed effects of simultaneous activation of multiple electrodes in the array. Implants in clinical use today (Argus II and the Alpha IMS) use a common remote return electrode, and previous studies [21–23] indicate that cross-talk from neighboring pixels could strongly reduce the contrast of the generated electrical pattern, and thereby limit the spatial resolution. Local spatiotemporal contrast of visual stimuli is a primary determinant of image perception [24, 25], and a decrease in the contrast transfer function from the camera to the stimulating electric field can negatively impact the ability of the prosthesis to convey meaningful visual information [26]. Poor confinement of the electric field increases cross-talk between neighboring pixels, thereby lowering the contrast of the stimulation pattern. It is therefore crucial to quantify the impact of various return electrode configurations on an implant's ability to deliver high contrast stimuli.

Contrast of the electrical pattern can be quantified with respect to the potential or electric field (current density) in the medium. However, these quantities do not relate directly to neural stimulation efficiency in multi-layered tissue. Therefore, a model converting the generated electric field into retinal activity is necessary for analysis of the implant transfer function.

We demonstrate that modeling of an electric field in electrolyte must take into account the dynamics of the capacitive electrode–electrolyte interface, which rapidly transitions from an equipotential boundary condition at the beginning of a stimulation pulse to a uniform current density on electrodes in steady state. When modeling a single stimulating electrode with a distant return, such change in boundary conditions has little effect. However, simultaneous activation of multiple electrodes in a dense array with local returns reveals the changes associated with this dynamic boundary condition. We verify our model's boundary conditions by mapping the electric potential in electrolyte above a photovoltaic array with 70 μm pixels.

We then quantify the differences in retinal response to electric fields generated by subretinal arrays with various return electrode configurations using a simple model of retinal response to network-mediated stimulation. Our results show that monopolar arrays with a common remote return have very poor field confinement. In an array with isolated local returns in each pixel, electric fields are over-confined, which prevents electric potential measurement on the corneal surface, thereby precluding post-implantation pixel diagnostics. An array with local returns in each pixel connected to one another provides a convenient compromise between these two extremes. Finally, we demonstrate that dividing the input image into sparse sequentially activated sub-frames [27] decreases pixel cross-talk and increases the electric field contrast in monopolar arrays, with little cost to stimulation selectivity.

2. Methods

We first define the procedures for modeling and measuring the electric field, including HSPICE assessment of the dynamics of the boundary conditions (section 2.1.1), COMSOL modeling of the spatial distribution of electric field in the medium (section 2.1.2), and experimental field mapping (section 2.1.3). We then describe the method for converting the simulated electric field produced by a subretinal array into retinal response.

2.1. Modeling and measuring electric field

2.1.1. Modeling in HSPICE. High-density neurostimulating arrays include multiple active stimulating electrodes and return electrodes [28], resulting in complex interactions between active and return. To assess the current redistribution dynamics between proximal and distal parts of a return electrode mesh, we study the simplified equivalent circuit (figure 1(A)) for a comparable electrode configuration (figure 1(B)). It includes a single active disk electrode (1) surrounded by two concentric ring return electrodes. The smaller adjacent ring (2) represents a local return immediately adjacent to the active electrode, while the larger and more

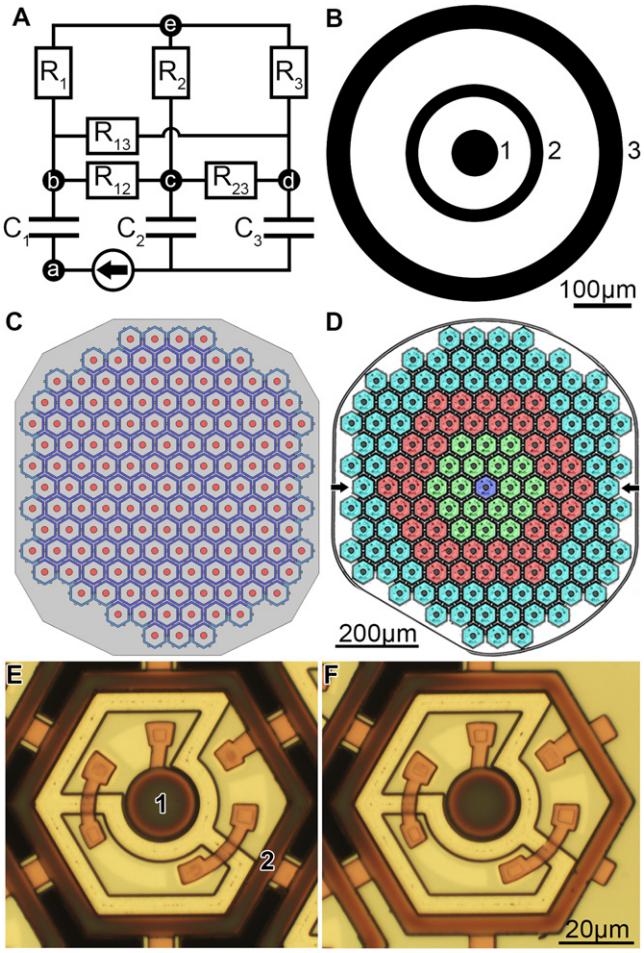

Figure 1. (A) Simplified equivalent circuit of a disc electrode with local and peripheral returns. The active (branch 1), local return (branch 2), and global return (branch 3) electrodes have a corresponding capacitance and electrolyte resistance derived from the COMSOL modeling. (B) Electrode geometry in COMSOL model used to calculate the medium resistance between the active (1), local return (2), and global return (3) electrodes. (C) Geometry of electrodes in the COMSOL model of photovoltaic array. Red regions signify active (current injecting) electrodes, while blue regions denote a mesh of return electrodes. (D) Fabricated retinal prosthesis with 142 pixels. Blue, green, red, and cyan regions represent pixels activated by beams of 1, 5, 9 and 13 pixels in width, respectively. (E) Pixel in the middle of the photovoltaic array. Regions 1 and 2 represent the active and local return electrodes, respectively. (F) Pixel at the periphery of the array. Variations in brown color of the electrodes indicate changes in SIROF thickness: darker color represents thicker layer.

distant ring (3) represents the rest of the return electrode mesh in the array. The electrodes are modeled as voltage-dependent capacitors [29], and interconnecting resistances (R_{xy}) and resistances to infinity (R_x) correspond to the electrolyte resistance. A 5 μA current source in the active branch provides 20 ms current pulses for this simulation.

Node *a* represents the active metal electrode potential. Potentials at nodes *b*, *c*, and *d* correspond to the medium just above the electrodes. Node *e* in this equivalent circuit represents a large Ag/AgCl reference electrode placed in electrolyte far from the electrode array. The potential difference between nodes *b*, *c*, *d* and the reference node *e* represent the potential measured in the medium near each electrode surface (active, local return, and peripheral return, respectively), relative to the reference electrode.

Interconnecting resistor values in the circuit were calculated using a finite element model solved in COMSOL Multiphysics 5.0, in which one electrode injects current *I*, while another electrode accepts the same current. The resistance between two electrodes is:

$$R_{x\to y} = \frac{V_x - V_y}{I}. \quad (1)$$

where V_x and V_y are potentials for the current injecting and returning electrodes of interest, respectively. We calculated the resistances between each electrode and the reference electrode at infinity, and then between each pair of electrodes: (1) the active (center) electrode and the local return; (2) the active electrode and the global return and (3) the local return and the global return. Resistive values from each electrode to infinity were calculated using the same model, but with the current *I* injected from an electrode and returning to a large equipotential boundary of the liquid domain at infinity. The resistance is then found by dividing the resulting potential at the electrode surface by the injected current.

2.1.2. Electric field in electrolyte: modeling in COMSOL. We assessed the electric field distribution in electrolyte in front of a photovoltaic array with various injected current patterns by solving a finite element model of the array in COMSOL Multiphysics 5.0, using the electrostatics module. Due to the complex electrode configuration in the array, all COMSOL simulations were static. Boundary conditions in COMSOL were derived from the HSPICE simulation for the comparable circuit described above.

We explored two boundary conditions for the active and return electrodes. (1) When the surface of each electrode was assumed to be equipotential, the COMSOL solver distributed the total injected current over each electrode such that the equipotential condition was met. (2) With the uniform current density boundary condition, the current density normal to the electrode surface was defined over each electrode by dividing the total injected current in each electrode over the corresponding electrode surface area. For both boundary conditions, we enforced charge balance by equating the total current at the return electrodes to the total current injected by the active electrodes. For all simulations, the zero reference voltage was set at the chamber sidewalls.

The modeled photovoltaic arrays are 1 mm in diameter, 30 μm thick, and are composed of 142 hexagonal pixels of 70 μm in width [20, 22, 30, 31] (figure 1(C)). Each pixel has a central, 18 μm diameter active disk electrode and 5 μm wide hexagonal circumferential return electrode. Pixels are separated by 5 μm wide gaps (figure 1(E)). All electrode surfaces are coated with sputtered iridium oxide film (SIROF). The outer pixel ring (adjacent to the boundary of the array) has a thinner SIROF coating compared to the central pixels (notice the lighter color in figure 1(F)), and therefore lower capacitance compared to the rest of the array.

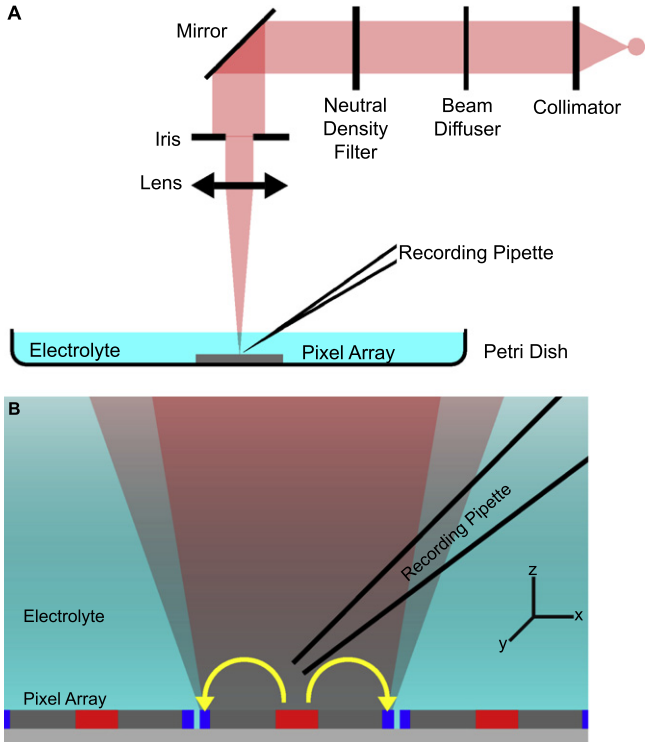

Figure 2. Diagram of the setup for measuring electric potential above the array. (A) Laser beam projected via the microscope. (B) Laser beam illuminating a single photovoltaic pixel in the array. Recording pipette translated laterally with 2 μm steps to map electric potential in the medium.

Under the uniform current density boundary condition, the outer pixel ring accepts a lower current density compared to the rest of the returns, proportional to its capacitance per unit area (total charge balance over the array is still preserved), as explained in section 3.2.

For comparison with experimental measurements, we computed the electric fields in electrolyte under four activation configurations (figure 1(D)), corresponding to the light spot sizes on the photovoltaic array of 1, 5, 9 and 13 pixels in width.

2.1.3. Electric potential mapping in electrolyte. We validated our finite element model by measuring the potential generated in front of the photovoltaic array placed in a Petri dish filled with a 17.1 mM NaCl solution ($\rho \approx 500\ \Omega$cm) and containing a large (1 mm) Ag/AgCl reference electrode. A borosilicate micropipette (opening diameter $\approx 1\ \mu$m) containing the Ag/AgCl wire was positioned 20 μm above the devices, and translated laterally and axially using a piezoelectric driver. Lateral translation of the pipette over the central row of the device (indicated by the arrows in figure 1(D)) was performed with 2 μm steps. Waveforms detected via the pipette electrode were recorded using a patch clamp amplifier (MultiClamp 700A, Axon Instruments) (figure 2). We averaged ten measurements at each position to improve the signal-to-noise ratio.

An 880 nm laser (DILAS M1F4S22) illuminated the photodiodes with 5 ms pulses at 5 Hz repetition rate for all four spot sizes. The laser beam projected through an open iris via a 4x objective was sufficiently wide to illuminate the entire device, with a 10% intensity variation between the center and the periphery.

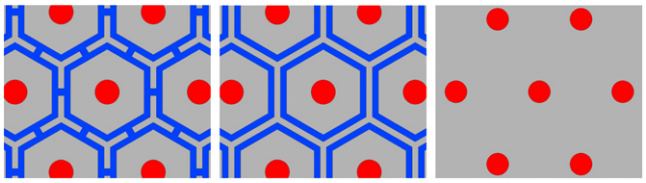

Figure 3. Three configurations of the return electrodes: left—connected local returns; middle—disconnected local returns; right—common remote return electrode on the back surface of the array.

2.2. Modeling retinal stimulation

2.2.1. Return configurations. We considered three different return electrode configurations in the array (figure 3)): connected local return mesh, isolated local returns, and a monopolar array with a large common return at the back side of the implant. In the connected configuration, the 5 μm wide hexagonal return electrodes surrounding each active electrode are electrically connected, creating a return electrode mesh that acts as a collective current sink. In the isolated configuration, individual pixel returns are not connected to their neighbors, and the current injected from the central active electrode is equal in value and opposite in sign to the current uniformly distributed over the adjacent return electrode in each pixel. In the monopolar configuration, the return electrode covers the back side of the implant. Monopolar electrode arrays used in retinal prostheses usually have an even more distant return electrode (e.g. on a power supply of the implant), but for wireless photovoltaic pixels, the most practical place for a remote return electrode is on the back side of the device. For all configurations, we applied the uniform current density boundary condition on each electrode surface to represent device behavior in steady state.

2.2.2. Electric field with grid patterns. Resolution and contrast sensitivity are often measured using grating patterns. We simulated the effect of grating patterns on the photovoltaic arrays by activating alternating pixel rows with various intensities: I_{max} (bright pixels) and I_{min} (dark pixels). In the common return configurations (connected and monopolar), the current flowing through the returns was equal to the total current injected through all active electrodes. Stimulating pattern contrast was defined by the Michelson contrast parameter

$$C = \frac{I_{max} - I_{min}}{I_{max} + I_{min}} \quad (2)$$

which varied between 0 and 1.

2.2.3. Modeling the retinal response. Activation thresholds for the RGCs and INL in terms of current density were taken from previously reported measurements of direct and

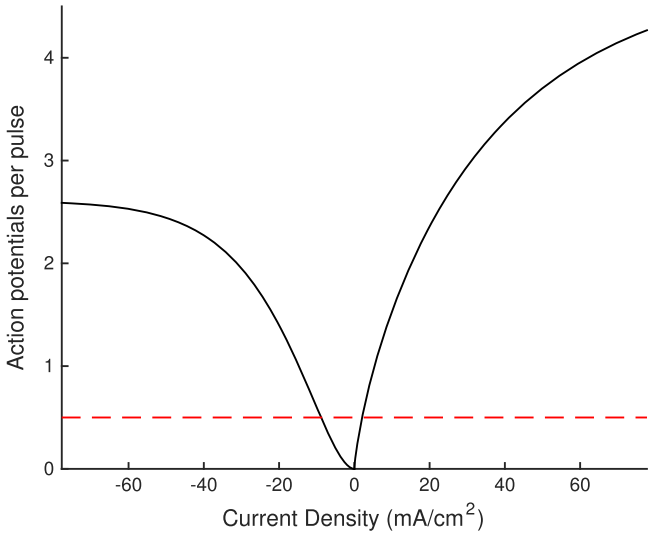

Figure 4. Responsivity of the retinal ganglion cells to network-mediated stimulation. Threshold is defined as 0.5 action potential per stimulus.

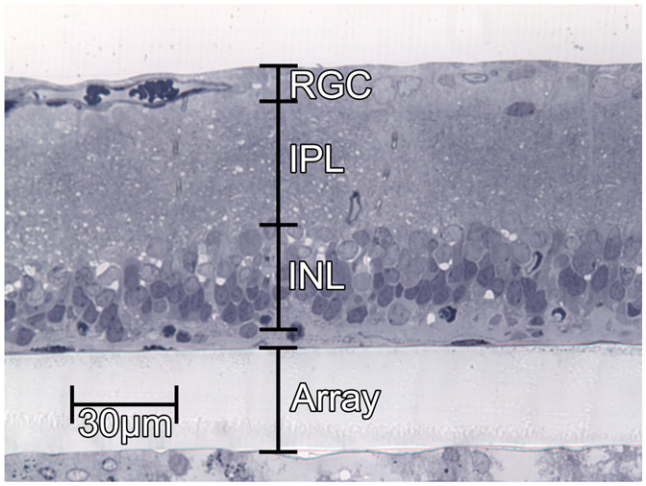

Figure 5. Histology of RCS retina with 30 μm thick subretinal plastic implant. IPL is the inner plexiform layer separating the inner nuclear layer (INL) from retinal ganglion cells (RGC).

network-mediated stimulation via large (>500 μm) electrodes [32]. Threshold was defined as the current density eliciting an action potential in RGCs with a 50% probability at pulse duration exceeding cell chronaxy. With a 5 ms stimulus, the threshold was 1 mA cm^{-2} for direct RGC stimulation, and 2 mA cm^{-2} for the INL-mediated response. We assumed that only the vertical (z) component of the current density factors into the cell responsivity, and the middle row of the implant served as the region of analysis.

Strength of the network-mediated retinal response was expressed by the number of the elicited action potentials in RGCs, based on the activation curve measured in rat retinas [20, 28], which was scaled to match the threshold values with 50% response probability, as shown in figure 4.

In degenerate rat retina (RCS), the INL extends between 5 and 35 μm above the array, while the ganglion cell layer (GCL) extends between 80 and 90 μm (figure 5) [33]. To

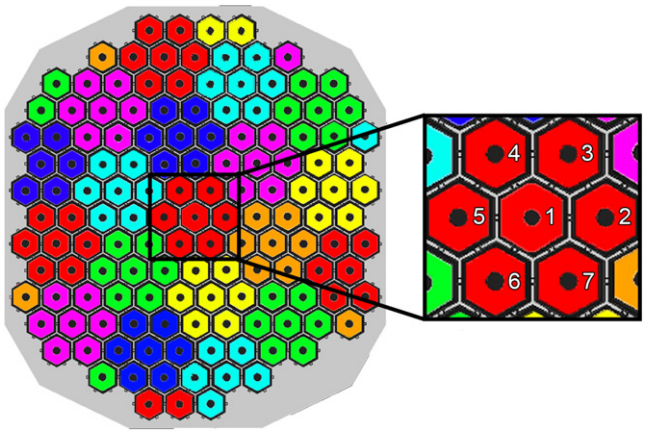

Figure 6. For sequential activation, pixels are clustered into hexagonal groups of seven (adjacent pixels with the same color), and pixels in each group are activated in a sequence of seven sub-frames, such that no more than one pixel is active per group.

asses retinal responses to electrical stimulation by each pixel, we multiplied the vertical current density at every point above the array by the corresponding INL responsivity value and integrated over the volume corresponding to the pixel size and thickness of the target cell layer (INL). For the network-mediated activation, the integration extended vertically from 5 to 35 μm.

Direct stimulation of RGCs with epiretinal arrays and network-mediated stimulation with subretinal implants encode visual information differently: the former by the number of pulses and their frequency and the latter by pulse amplitude and duration. Hence, selective activation of the INL or GCL is desirable for each strategy. For a subretinal implant, activation of the INL should avoid eliciting direct responses in the RGCs. For each stimulation pattern, current density in the RGC layer should therefore remain below the direct stimulation threshold. Thus, for each device configuration, the $I_{\max}$ in the bright pixels was set to avoid direct stimulation of RGCs by ensuring the current density in the RGC layer stayed below 1 mA cm^{-2}.

The INL-mediated RGC activity in the bright and dark areas was calculated as the mean of the responses over bright and dark pixels along the middle row of the device, respectively:

$$N_{\text{bright}} = \frac{\sum_i^N N_{\text{bright}_i}}{N},$$
$$N_{\text{dark}} = \frac{\sum_j^K N_{\text{dark}_j}}{K}, \quad (3)$$

where N and K represent the number of bright and dark pixels in the middle row ($N = 6$, $K = 5$), and N_{bright_i} and N_{dark_j} is the retinal responsivity for the ith and jth bright and dark pixel, respectively.

2.2.4. Sequential activation of pixels. The electric field generated during sequential activation of several sub-frames in the array was calculated by clustering pixels into groups

containing sequentially activated electrodes. For hexagonal arrays, the natural group includes seven pixels (figure 6). Individual electrodes in each group are then activated sequentially, such that only one electrode is active per group per sub-frame. The combined activation of all seven sub-frames yields an input identical to the previously described full-frame pattern.

To quantify the retinal response to this segmented stimulation, we first carry out the same analysis of converting the calculated current density to neural activity for each sub-frame, and then take the maximum response per pixel across all sub-frames. The Michelson contrast between the average of all bright pixels and the average of all dark pixels is calculated as

$$C = \frac{\frac{\sum_i^N \max(N_{\text{bright}_i})}{N} - \frac{\sum_j^K \max(N_{\text{dark}_j})}{K}}{\frac{\sum_i^N \max(N_{\text{bright}_i})}{N} + \frac{\sum_j^K \max(N_{\text{dark}_j})}{K}}. \quad (4)$$

3. Results

3.1. Dynamics of current redistribution on an extended return electrode

Using the circuit shown in figure 1(A), we simulated the current redistribution dynamics during a stimulation pulse delivered into the medium via SIROF electrodes. With a central disk electrode of 80 μm in diameter, a local return electrode of 200 and 240 μm inner and outer diameters, and a peripheral return electrode of 440 and 520 μm inner and outer diameters, respectively, in a medium with 0.2 Sm^{-1} conductivity (500 Ωcm resistivity), the circuit parameters are: $R_1 = 31.1\ \text{k}\Omega$, $R_2 = 11.3\ \text{k}\Omega$, $R_3 = 5.3\ \text{k}\Omega$, $R_{12} = 30.7\ \text{k}\Omega$, $R_{13} = 32.4\ \text{k}\Omega$, $R_{23} = 10.4\ \text{k}\Omega$, $C_1 \approx 50.3$ nF, $C_2 \approx 138$ nF, and $C_3 \approx 736$ nF.

As shown in figure 7(A), the potentials above the local and peripheral return electrodes start deviating from the beginning of a pulse. Within about 3 ms, the potentials approach different steady-state values of -0.5 mV and -8.2 mV.

As can be seen in figure 7(B), the local return initially accepts higher current density compared to the peripheral return. The smaller capacitance of the local return electrode is quickly charged, and therefore its potential rises faster than that of the larger peripheral return (figure 7(C)). The potential rise rates and the corresponding current densities on return electrodes equalize within 3 ms (exponential time constant $\tau = 0.8$ ms), and remain constant for the rest of the pulse. If the interface capacitance per unit area c is the same, the equal rates of the potential rise correspond to the same uniform current density j on each return electrode:

$$\frac{dV}{dt} = \frac{j}{c}. \quad (5)$$

However, if the capacitance per unit area of one return electrode is lower, the current density will be similarly reduced to provide the same rate of the potential rise. At the end of the pulse, electrodes are recharged following similar dynamics with an opposite polarity (figure 7).

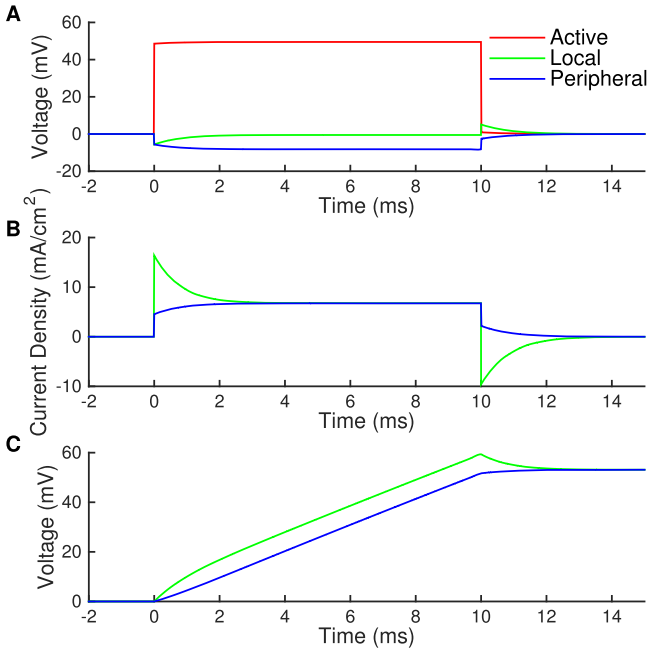

Figure 7. Dynamics of the current redistribution between active, local return, and peripheral return electrodes computed in HSPICE. (A) Potentials in the medium above the electrodes (nodes *b*, *c* and *d*) relative to the reference electrode (node *e*). (B) Current density on the local and peripheral return electrodes. Initially different, they converge during the first 2 ms. (C) Potential across the local return capacitance (*C*2) initially rises faster than on peripheral return (*C*3), but the rate equalizes within 2 ms.

The current redistribution time course is set by the circuit time constant ($\tau = RC$) with respect to the local electrode. For capacitance $C = 51$ nF, and $\tau = 0.8$ ms, the equivalent resistance seen by the local return electrode is 16 kΩ. Electrolytes with higher conductivities and electrodes with lower capacitance per unit area reach steady state faster. For example, electrodes with the same geometry as described above, but immersed in saline with higher conductivity (70 Ωcm resistivity), reach steady state within 0.3 ms instead of 2 ms.

3.2. Electric field produced by the array

We measured the electric potential in electrolyte 20 μm above the array having connected local returns after it reached steady state. The potential measured across the central pixel row with four different activation spot diameters is shown in figure 8. To eliminate dependence on light intensity, the measured voltages for all spot sizes are normalized to the maximum voltage produced by single pixel illumination. Increasing the activation spot size diameter from one to five pixels increases the maximum potential above the central pixel by a factor of 3. A further increase to a nine-pixel wide spot decreases the normalized potential in the center to 2.3, while illuminating the full array leads to a negative potential in the center. The electric potential in the electrolyte

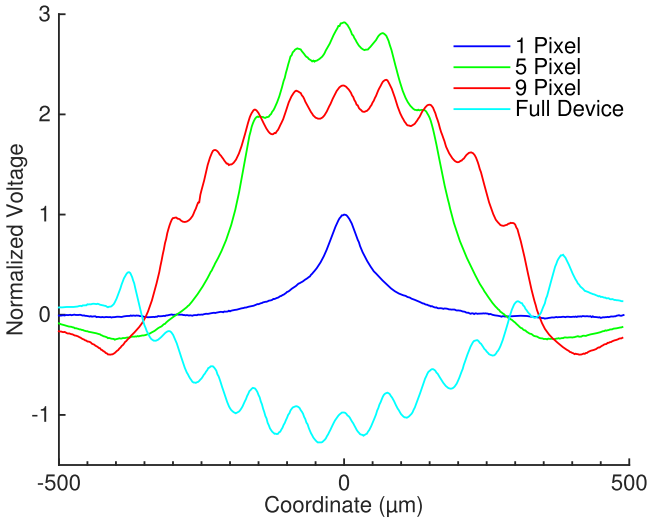

Figure 8. Experimentally measured potential in the medium above the photovoltaic array for various beam sizes, normalized to potential above the single illuminated pixel. Widening the spot from 1 to 5 pixels increases the potential, but further beam expansion decreases it.

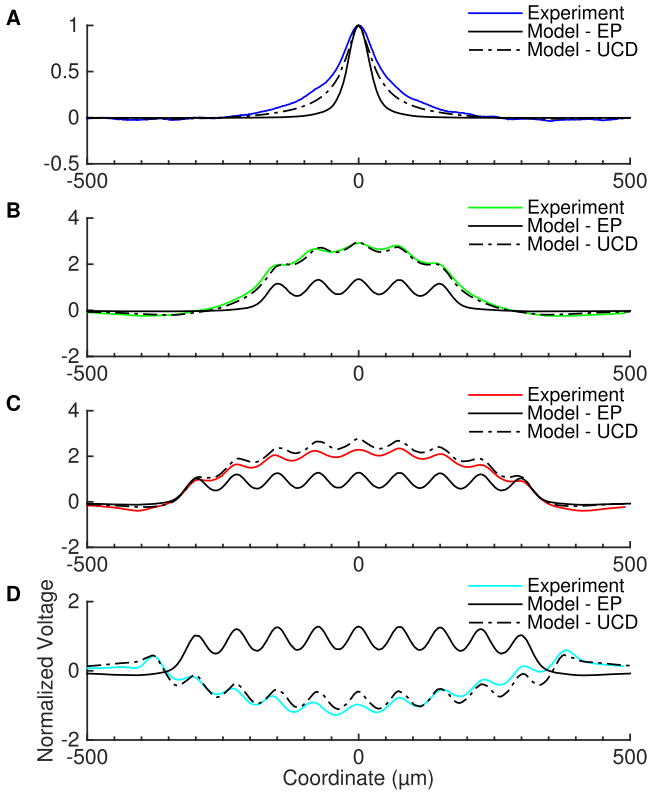

Figure 9. Comparison of the experimental results (color) with computational models utilizing an equipotential (EP, solid) and uniform current density (UCD, dash) boundary conditions for the beam sizes described in figure 1(D). Unlike with equipotential boundary conditions, modeling with the uniform current density matches all the features of the experimental data.

calculated with a COMSOL model for two boundary conditions (equipotential and uniform current density) is shown in figure 9 alongside the experimental measurements. The uniform current density model reproduces the initial increase and

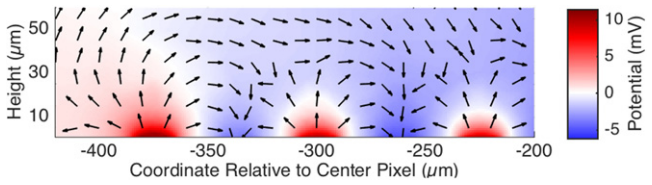

Figure 10. Potential (color map) and current (arrows) above the three peripheral pixels in the central row of the array. Due to reduced capacitance of the local return electrode at the edge of the array, peripheral pixels cannot locally return their injected current, and it flows towards the more central areas. This effect increases the negative potential of the returns in the center.

subsequent decrease of the potential in front of the device upon widening of the illumination spot. The model with equipotential electrodes, however, does not reproduce experimental results. In particular, the potential in front of the device does not increase enough with partial illumination, and does not invert under full-field illumination (figure 9).

The rise in potential with an increase in beam size from one to five pixels comes from two effects: (1) summation of the current from adjacent pixels, accounted for with both boundary conditions, and (2) an additional rise in the model with uniform current density due to the current spread over a wide return electrode mesh. Unlike very local return of current with equipotential electrodes, with uniform current density, the injected current spreads much farther—over the entire device, resulting in an increase in the potential above the active pixels.

When the number of active pixels increases further, the effect of the return electrode becomes more pronounced. Current density on the return electrode increases and its potential is drawn more and more negative. Illumination of the whole array (figure 9(D)) produced negative potential in the center because the return electrode mesh around the peripheral pixels has a very low capacitance, which forces the current from these pixels towards the central portion of the return mesh (figure 10). Devices with the same capacitance on all parts of the return electrode do not produce a negative potential in the center under full array illumination.

Current redistribution over the return electrode mesh depends on the extent of array utilization, i.e. on projected light pattern density and intensity. Therefore, the amplitude and contrast of the corresponding electrical pattern are affected by the projected image structure. We assess the implications of these phenomena for retinal stimulation in the next section.

3.3. Modeling arrays with various return configurations

Electric field distribution in front of the array is markedly different for bipolar and monopolar configurations (figure 11). The absence of local returns in the monopolar array forces the injected current to flow to the back side, which results in a potential build-up in front of the device. Near each pixel (within the pixel radius), current spreads radially from the active electrode. Beyond the pixel radius, currents add-up and the whole array acts as one large electrode, with its electric field (current density) slowly decreasing with increasing distance from the array (figure 11(C)). Introducing local return

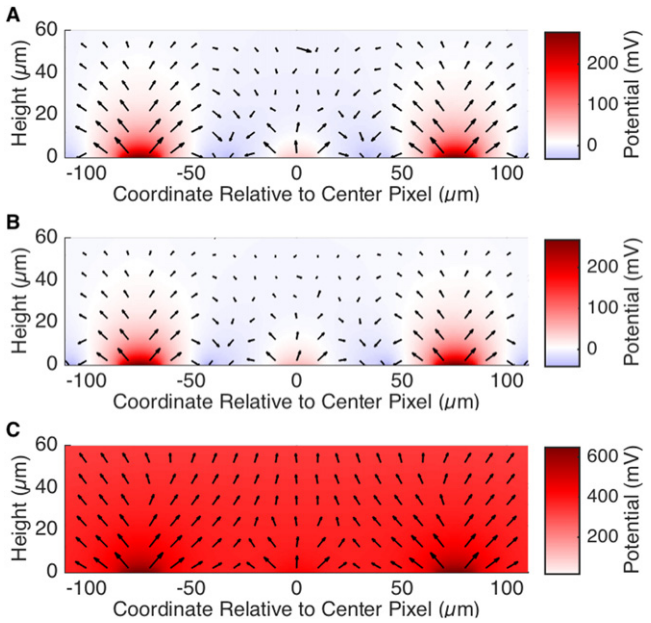

Figure 11. Potential (color map) and current (arrows) above the central three pixels in the middle row of the array for isolated (A), connected (B), and monopolar (C) return configurations. Central pixel is 'dark' (current $I_{min} = 0.2\ \mu A$) and adjacent ones are 'bright' (current $I_{max} = 1\ \mu A$) in the grid pattern. Arrays with local returns confine the current and potential above the device much better than the monopolar configuration with the same input.

electrodes eliminates this large potential build-up. The resulting current density and potential decrease much faster with distance from the array (figures 11(A) and (B)).

In bipolar arrays with isolated returns, the injected current is drained back to the local return electrode in the same pixel, which confines the electric field much more than for the array with connected returns. In the latter case, the current injected by a single active electrode can spread over the whole 1 mm-wide return mesh. The wider current spread in this configuration results in a slower decrease of the electric field with distance. A single activated pixel in the connected bipolar and monopolar arrays generates potentials 1 mm away from the device that are two and three orders of magnitude greater than the potential generated by the isolated pixel, respectively (figure 12). With the electric field slowly decreasing with distance from the implant, it is possible to detect signals generated by single pixels on the cornea, which enables monitoring pixel performance in the implanted arrays over time [34].

3.4. Retinal response to patterned electric field

Network-mediated retinal response above the bright and dark subretinal pixels is plotted (in the number of spikes per stimulus) as a function of contrast for three device configurations in figure 13(A). Monopolar arrays can elicit very little network-mediated activity below the direct RGC stimulation threshold, defined as the 50% probability of activating the cell, due to poor electric field confinement in the axial (vertical) direction. Isolated returns provide the best confinement,

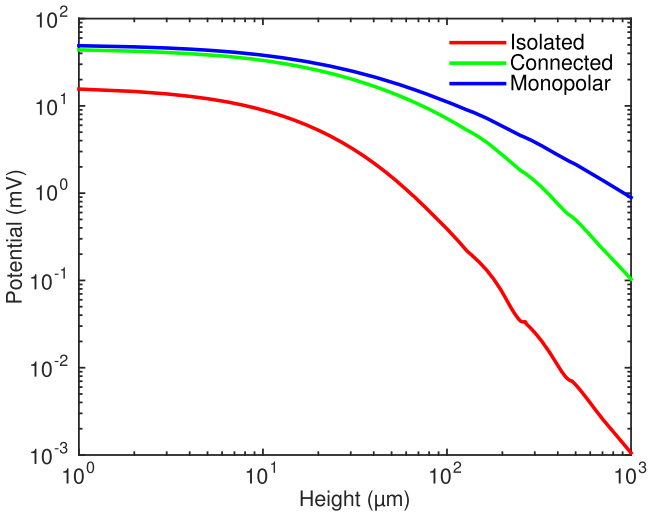

Figure 12. Potential as a function of height above the single activated pixel. One millimeter above the array, a pixel with isolated returns generates a potential three orders of magnitude lower, and with connected returns—1 order of magnitude lower than that of a monopolar pixel (1 μV 100 μV, and 1 mV, respectively).

and therefore allow the highest injectable current and strongest retinal response. Connected returns provide less confinement than isolated electrodes and are therefore restricted to lower currents before activating the RGCs, which reduces the tissue response.

Having a model for the mean responses to bright and dark pixels, we can calculate the contrast of the retinal response as

$$C = \frac{N_{\text{bright}} - N_{\text{dark}}}{N_{\text{bright}} + N_{\text{dark}}}. \tag{6}$$

The output contrast for all three array configurations is plotted in figure 13(B) as a function of the input contrast, and each curve is color coded according to the maximum activity elicited by the bright pixels. The calculated output contrast is lower than unity (i.e. ideal transfer function with output contrast = input contrast) for all three device configurations. For both bipolar configurations, the output contrast is greater than the corresponding values for the monopolar array by about 30%. The monopolar configuration can only elicit a very low number of action potentials above the bright pixels while staying below the direct RGC activation threshold.

As shown in figures 13(C) and (D), sequential activation of sparse patterns greatly improves the number of spikes elicited by the monopolar array while avoiding direct RGC stimulation. Reduction in the pattern density to, at most, 1/7th of the total decreases the build-up of the vertical current in front of the device. This allows for higher current injection compared to simultaneous activation, as the current density at the RGC layer is reduced.

4. Discussion

Ideally, retinal prostheses should provide stimulation to target cells with high resolution and wide dynamic range. The

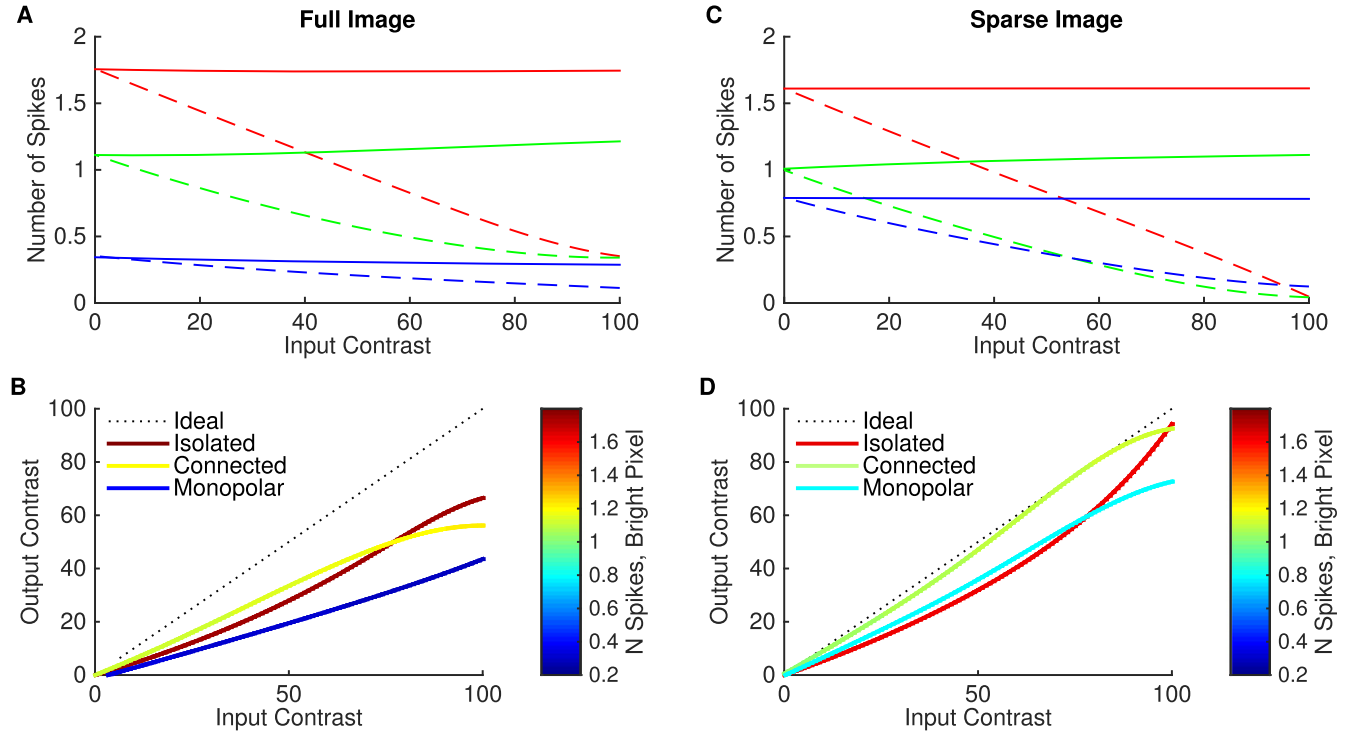

Figure 13. Retinal network-mediated response for a full image (A) and (B), and sequential, sparse image (C) and (D) activation. (A) Number of spikes as a function of input contrast for pixels injecting I_{max} (solid) and I_{min} (dash). The strong field confinement of the isolated (red) pixels allows for the highest injected current without direct RGC stimulation. Connected (green) arrays are limited by smaller current, eliciting lower INL-mediated response, while monopolar (blue) arrays cannot exceed the 0.5 spike threshold. (B) Output contrast as a function of input contrast, with line color representing the number of spikes generated by bright pixel. Isolated and connected configurations perform similarly, while monopolar exhibits poorer contrast and much lower number of spikes. (C) Sequential activation of the pixels improves performance of the monopolar array. (D) Contrast improved for all configurations in sequential activation, although the major beneficiary is the monopolar array.

electric field should be tightly confined not only laterally to provide high spatial resolution and low cross-talk but also axially to avoid stimulating cells outside the target layer. Developing accurate computational models of the electric field generated by a multielectrode array helps design implants that meet these criteria. The equipotential boundary condition commonly used in the literature [22, 35] is inadequate since electric currents redistribute over time on extended electrode surfaces. Strictly speaking, no static boundary conditions [36] can properly describe the dynamics of the electrode–electrolyte interface, and therefore will not fully represent the field generated by an electrode array.

At the beginning of the pulse, an electrode is equipotential and the current density on its surface is uneven. Currents flow along the path of least resistance to the nearby return, and the current density is therefore highest at the edges of an equipotential electrode. The capacitive electrode–electrolyte interface charges up faster in areas with higher current density, thereby changing the electric potential distribution in electrolyte. Over time, the system reaches steady state, where the potential in the electrolyte facing all electrode surface regions rise at the same rate. If the capacitance per unit area is uniform over the surface of the electrode, this condition corresponds to a uniform current density. If some electrode regions have a different capacitance, the current density over these areas will be proportional to ensure the same rate of potential rise.

The duration of the transition from equipotential to uniform current density depends on the resistances and capacitances involved. Our HSPICE model shows that the RC time is dominated by the local return capacitance and by the resistance between the active and local return electrodes. For example, the capacitance of a polished metal return electrode ($c \approx 10\ \mu\text{F cm}^{-2}$) in our hexagonal configuration (80 μm outer diameter, 5 μm) is about 100 pF, and the resistance in saline ($\rho \approx 70\ \Omega\text{cm}$) is about 20 k$\Omega$. Therefore, the characteristic electrode charging time is on the order of 1 μs. With a SIROF coating ($c \approx 10\ \mu\text{F cm}^{-2}$) and the same electrode geometry, the capacitance will increase to about 10 nF, and in tissue ($\rho \approx 500\ \Omega\text{cm}$), the resistance will increase to about 100 kΩ, resulting in a charging time on the order of 1 ms. Redistribution of the current density in neural stimulation, therefore, will depend on electrode geometry, materials, and pulse duration.

Many electrode arrays for retinal stimulation have a monopolar configuration, with a remote common return electrode [16, 37, 38]. If many electrodes are activated simultaneously, the electric fields in front of monopolar arrays add-up, resulting in strong interference from the neighboring electrodes and reduced field confinement, as illustrated in figure 11(C). One way to reduce cross-talk and improve field

confinement is by introducing a local return electrode in each pixel [39].

An electrode array with isolated local returns provides the best field confinement out of the configurations we studied. However, the surface area of the local return electrode should be much larger than the active electrode in order to minimize the voltage drop in front of the return electrode. In the case of a photovoltaic array, this requirement reduces the open silicon area for light collection and will therefore reduce the maximum current output per pixel. It also decreases the distance between the active and return electrodes, which will increase field confinement in the axial dimension, making it harder to reach the target cell layer.

A mesh of connected local return electrodes offers a compromise between the two extremes: (1) tight confinement with isolated returns and (2) poor confinement with monopolar electrodes. This configuration still strongly reduces cross-talk between neighboring electrodes, thereby improving the generated pattern contrast and maximum pixel brightness below the direct RGC activation threshold, compared to monopolar arrays. By connecting the local returns, the area of the return electrode per pixel can be reduced without detrimentally increasing the voltage drop at the return, since images delivered to a subretinal implant will likely be sparse in order to ensure efficient delivery of visual information [26]. For a photovoltaic array, reducing the return electrode area makes it possible to increase the photosensitive area and thereby improve the light collection capability of each pixel. Another benefit of the connected return mesh is that, unlike pixels with isolated returns, the electric field decreases with distance slowly enough to induce a measurable potential on the cornea, which enables monitoring the implant performance over time.

Sequential activation of pixel groups in the array, although technically more difficult than simultaneous stimulation, reduces the total injected current and thereby helps preventing direct RGC activation. Reducing the number of simultaneously activated neighbors also improves the perceived contrast with monopolar arrays. With a photovoltaic prosthesis, sequential activation may be easily achieved by dividing the projected image into multiple sub-frames that are projected sequentially [27].

5. Conclusions

Extended electrodes transition from an equipotential boundary condition at the beginning of a pulse to uniform current density in steady state. The electric fields generated by dense monopolar arrays with a remote return are poorly confined in the axial direction, and therefore tend to indiscriminately activate all neural layers in the retina. A mesh of connected return electrodes surrounding each pixel confines the field and enables more targeted inner retinal stimulation while avoiding direct activation of ganglion cells. An isolated local return electrode in each pixel provides the best field confinement, but it over-constrains the field to such an extent that it cannot be measured on the cornea, thereby preventing device diagnostics after implantation. Sequential activation of the stimulating electrodes may improve performance of the monopolar devices, and the extent of improvement depends on the number of simultaneously activated pixels.

Acknowledgments

We would like to thank Drs Ted Kamins, Keith Mathieson, and James Harris and Ludwig Galambos for help with fabrication of the photovoltaic arrays, as well as Dr David Boinagrov for help with potential field mapping. Supported by the National Institutes of Health (Grant R01-EY-018608), the Department of Defense (Grant W81XWH-15-1-0009), a Pixium Vision research grant, and the Stanford Neurosciences Institute (Interdisciplinary Scholar award to G.G.).

References

[1] Navarro X, Krueger T B, Lago N, Micera S, Stieglitz T and Dario P 2005 *J. Peripher. Nervous Syst.* **10** 229–58
[2] He B 2005 *Neural engineering* (New York: Kluwer)
[3] Wilson B S and Dorman M F 2008 *J. Rehabil. Res. Dev.* **45** 695–730
[4] Ho A C *et al* 2015 *Ophthalmology* **122** 1547–54
[5] Ghezzi D 2015 *Frontiers Neurosci.* **9** 290
[6] Jackson A and Zimmermann J B 2012 *Nat. Rev. Neurol.* **8** 690–9
[7] Zimmermann J B and Jackson A 2014 *Frontiers Neurosci.* **8** 87
[8] Pons J, Rocon E, Ceres R, Reynaerts D, Saro B, Levin S and Van Moorleghem W 2004 *Auton. Robots* **16** 143–63
[9] Bressler N M, Bressler S B and Fine S L 1988 *Surv. Ophthalmology* **32** 375–413
[10] Jager R D, Mieler W F and Miller J W 2008 *New England J. Med.* **358** 2606–17
[11] Santos A, Humayun M S, de Juan E, Greenburg R J, Marsh M J, Klock I B and Milam A H 1997 *Arch. Ophthalmology* **115** 511–5
[12] Milam A H, Li Z Y and Fariss R N 1998 *Prog. Retinal Eye Res.* **17** 175–206
[13] Mazzoni F, Novelli E and Strettoi E 2008 *J. Neurosci.* **28** 14282–92
[14] Rizzo J F and Wyatt J 1997 *Neuroscientist* **3** 251–62
[15] Ahuja A *et al* 2011 *Br. J. Ophthalmology* **95** 539–43
[16] Zrenner E *et al* 2011 *Proc. R. Soc.* B **278** 1489–97
[17] Fried S I, Lasker A C, Desai N J, Eddington D K and Rizzo J F 2009 *J. Neurophysiol.* **101** 1972–87
[18] Jepson L H, Hottowy P, Weiner G A, Dabrowski W, Litke A M and Chichilnisky E 2014 *Neuron* **83** 87–92
[19] Jepson L H, Hottowy P, Mathieson K, Gunning D E, Dabrowski W, Litke A M and Chichilnisky E 2014 *J. Neurosci.* **34** 4871–81
[20] Lorach H *et al* 2015 *Nat. Med.* **21** 476–82
[21] Palanker D, Vankov A, Huie P and Baccus S 2005 *J. Neural Eng.* **2** S105
[22] Loudin J, Simanovskii D, Vijayraghavan K, Sramek C, Butterwick A, Huie P, McLean G and Palanker D 2007 *J. Neural Eng.* **4** S72
[23] Wilke R, Moghadam G K, Lovell N, Suaning G and Dokos S 2011 *J. Neural Eng.* **8** 046016
[24] Rucci M and Victor J D 2015 *Trends Neurosci.* **38** 195–206

[25] Shapley R M and Lam D M K 1993 *Contrast Sensitivity* vol 5 (Cambridge, MA: MIT Press)
[26] Goetz G *et al* 2015 *Investigative Ophthalmology Vis. Sci.* **56** 7186–94
[27] Goetz G, Mandel Y, Manivanh R, Palanker D and Čižmár T 2013 *J. Neural Eng.* **10** 056021
[28] Mathieson K *et al* 2012 *Nat. Photon.* **6** 391–7
[29] Boinagrov D *et al* 2016 *IEEE Trans. Biomed. Circuits Syst.* **10** 85–97
[30] Wang L *et al* 2012 *J. Neural Eng.* **9** 046014
[31] Loudin J D, Cogan S F, Mathieson K, Sher A and Palanker D V 2011 *IEEE Trans. Biomed. Circuits Syst.* **5** 468–80
[32] Jensen R J, Ziv O R and Rizzo J 3rd 2005 *Investigative Ophthalmology Vis. Sci.* **46** 1486–96
[33] Lorach H *et al* 2015 *Investigative Ophthalmology Vis. Sci.* **56** 4644–52
[34] Lorach H, Goetz G, Mandel Y, Lei X, Kamins T I, Mathieson K, Huie P, Dalal R, Harris J S and Palanker D 2015 *Vis. Res.* **111** 142–8
[35] Djilas M *et al* 2011 *J. Neural Eng.* **8** 046020
[36] Joucla S and Yvert B 2012 *J. Physiol.-Paris* **106** 146–58
[37] Zhou D D, Dorn J D and Greenberg R J 2013 The argus® ii retinal prosthesis system: an overview *2013 IEEE Int. Conf. on Multimedia and Expo Workshops (ICMEW)* (Piscataway, NJ: IEEE) pp 1–6
[38] Ayton L N *et al* 2014 *PloS One* **9** e115239
[39] Matteucci P B, Barriga-Rivera A, Eiber C D, Lovell N H, Morley J W and Suaning G J 2016 *Investigative Ophthalmology Vis. Sci.* **57** 1031–7